International Journal of Heat and Fluid Flow 117 (2026) 110129

Contents lists available at ScienceDirect

International Journal of Heat and Fluid Flow

journal homepage: www.elsevier.com/locate/ijhff

Flow-induced vibration of an elastically mounted oblate spheroid with variable mass ratio ☆

Adrian Cordero Obando [a,*], Kerry Hourigan [a], Mark C. Thompson [a], Jisheng Zhao [a,b]

[a] Fluids Laboratory for Aeronautical and Industrial Research (FLAIR), Department of Mechanical and Aerospace Engineering, Monash University, Clayton, 3800, VIC, Australia

[b] School of Engineering and Technology, The University of New South Wales, Canberra, 2600, ACT, Australia

ARTICLE INFO

Keywords:
Flow-induced vibration
Vortex-induced vibration
Galloping
Spheroids

ABSTRACT

This study experimentally investigates the cross-flow flow-induced vibration (FIV) of an elastically mounted oblate spheroid with an aspect ratio of 2. The aspect ratio is defined as the ratio of the major diameter (b) in the cross-flow direction to the minor diameter (a) in the streamwise direction, namely $\epsilon = b/a$. The FIV response was characterised over a range of reduced velocity, $3.0 \leqslant U^* = U/(f_{nw}b) \leqslant 12.0$, where U is the free-stream velocity and f_{nw} is the natural frequency of the system in quiescent water. The corresponding Reynolds number varied over the range $5000 \leqslant Re = Ub/\nu \leqslant 20\,000$, with ν denoting the kinematic viscosity of the fluid. The mass ratio of the hydro-elastic system, defined as the ratio of the total oscillating mass (m) to the displaced fluid mass (m_d), namely $m^* = m/m_d$, was varied from 32 to 250, while the mass-damping parameter $(m^*+C_A)\zeta$ was kept almost constant at 0.20 for all the m^* values tested, with C_A being the potential added-mass coefficient. The results reveal that the dynamic response exhibits two distinct FIV phenomena: vortex-induced vibration (VIV) and galloping-like vibration. The VIV region is characterised by a roughly bell-shaped and bounded amplitude of vibration response as a function of reduced velocity. The peak normalised vibration amplitude was observed to be $A^*_{10} = 0.70$. On the other hand, the galloping region is characterised by a linear increase in the amplitude response with increasing U^* beyond a critical value of $U^* = 7.0$, reaching a maximum value of $A^*_{10} \approx 2$ at the highest reduced velocity tested $U^* = 12$. Interestingly, maintaining a constant value for $(m^*+C_A)\zeta$ while varying m^* results in a maximum amplitude response almost identical across a wide range of m^*, similar to VIV of circular cylinders. Moreover, it was found that $m^* = 32$ displayed a hard-galloping-like (i.e. the onset of vibration triggered by a finite amplitude disturbance) response, while for $m^* \geqslant 50$ the response was characterised by a soft-galloping-like (i.e. small-amplitude excitation from rest) response.

1. Introduction

Flow-induced vibration (FIV), a subject of fluid–structure interaction (FSI), finds significant applications across various engineering areas, including oil risers, offshore platforms and structures, as well as high-rise buildings and bridges (see Hourigan et al., 2026). Fundamental FIV research has primarily focused on two-dimensional bluff bodies, such as slender cylinders, which are constrained to one or two degrees of freedom of motion. However, three-dimensional bluff bodies, such as spheroids, have also garnered interest, although they have been studied to a lesser extent (e.g. Williamson and Govardhan, 2004).

Two phenomena typical of FIV and of particular interest in this investigation are: *vortex-induced vibration* (VIV) and *galloping*. Depending on their excitation sources, VIV is described as an *instability-induced excitation* (IIE). It is noteworthy, however, that the onset of lock-in can be also interpreted as a coupled-mode flutter of the wake–structure system (Facchinetti et al., 2004; de Langre, 2006; Han et al., 2023a). On the other hand, galloping is described as a *movement-induced excitation* (MIE) (Naudascher and Rockwell, 2005).

VIV arises from the vortex shedding into the wake of a structure, inducing a fluctuating pressure distribution and causing self-limited structural vibration (see Bearman et al., 1987; Parkinson, 1989; Sarpkaya, 2004; Païdoussis et al., 2010). One of the most significant characteristics of VIV is the synchronisation (also known as "lock-in") between the structural vibration frequency and the vortex shedding frequency, which can result in significant vibration within a range of reduced velocity. On the other hand, galloping arises due to the induced aerodynamic force associated with the structure movement and

☆ This article is part of a Special issue entitled: 'AFMC 2024' published in International Journal of Heat and Fluid Flow.

* Corresponding author.
E-mail address: adrian.corderoobando@monash.edu (A. Cordero Obando).

https://doi.org/10.1016/j.ijheatfluidflow.2025.110129
Received 15 May 2025; Received in revised form 18 September 2025; Accepted 23 October 2025
Available online 24 November 2025
0142-727X/© 2025 Elsevier Inc. All rights are reserved, including those for text and data mining, AI training, and similar technologies.

supporting the structure movement (that is, aligned with the structure movement velocity).

For structures susceptible to MIE instability, an initial perturbation may trigger the galloping response, leading to a vibration growth with increasing flow velocity. This vibration response typically displays an unbounded monotonic increase of the vibration amplitude with increasing value of reduced velocity beyond a certain threshold value of reduced flow velocity, while the vibration frequency may be many times lower than the vortex shedding frequency (see Bearman et al., 1987; Nemes et al., 2012; Zhao et al., 2014, 2018a,c). Under certain geometric and flow conditions, the combined effect of VIV and galloping may occur, resulting in complex dynamics of the fluid–structure interaction (see Nemes et al., 2012; Zhao et al., 2014, 2018c).

Previous studies have shown that the afterbody (i.e. the structural part of a body downstream of the flow separation points) is a key factor affecting the responses of VIV, galloping, and combined VIV-galloping effect. For example, Nemes et al. (2012) and Zhao et al. (2014) demonstrated the influence of angle of attack on the FIV response of a square cylinder with low mass-damping ratios, revealing a rich variety of FIV response regimes and wake modes, such as sub-harmonic synchronisations and mode competitions. Subsequently, the experimental study of Zhao et al. (2018a) indicated that although an afterbody significantly influences the FIV response of a D-section cylinder, it is not essential for the occurrence of VIV at low mass-damping ratios. This challenged the conventional view in the literature that a D-section shape could not exhibit VIV due to its lack of an afterbody (e.g. the pioneering study by Brooks (1960)). The view of Zhao et al. (2018a) is further supported by the very recent numerical simulations of Gupta et al. (2025).

Nevertheless, significant research has been conducted on FIV of bluff bodies with geometries deviating from standard circular cylinders, such as elliptical cylinders. For example, Yogeswaran et al. (2014) found in their numerical investigation of VIV of elliptical cylinders in laminar flow at low Reynolds numbers, $60 \leqslant Re \leqslant 140$, that the peak vibration amplitude increased as the aspect ratio was increased from 0.7 to 1.43. Here, the aspect ratio is defined as the ratio of major diameter (b) in the cross-flow direction to the minor diameter (a) in the streamwise direction at zero incidence angle, namely $\epsilon = b/a$; the Reynolds number is defined by $Re = Ub/\nu$, with U being the free-stream velocity and ν the kinematic viscosity of the fluid. The numerical simulations at a fixed low Reynolds number of $Re = 100$ by Leontini et al. (2018) showed that the FIV response and wake modes of an elliptical cylinder of $\epsilon = 1.5$ depend on flow reduced velocity ($U^* = U/(f_n b)$) and the angle of attack, where f_n is the natural frequency of the oscillator system. Later, Zhao et al. (2019a) experimentally investigated the FIV response of elliptical cylinders with ϵ varying from 0.67 to 1.50 in an intermediate Reynolds number range of $860 \leqslant Re \leqslant 8050$; they found that the peak vibration amplitude of the $\epsilon = 1.50$ increased almost 100% ($1.56b$) over the circular cylinder case. More recently, the experimental study of Lo et al. (2023) showed that a thin elliptical cylinder of $\epsilon = 5$ exhibited an extreme hyper-branch response with its largest vibration amplitude reaching $7.8b$ (limited by the capacity of the experimental rig). These previous studies have indicated the influence of the elliptical ratio (ϵ) of elliptical cylinders on their FIV responses.

While extensive studies have been conducted on VIV of spheres as generic three-dimensional bodies (e.g. Govardhan and Williamson, 1997, 2005; Jauvtis et al., 2001; Sareen et al., 2018a,b,c; McQueen et al., 2021), FIV of spheroid remains largely unexplored. The recent study of Cordero Obando et al. (2024) showed that oblate spheroids with cross-sectional aspect ratios (also denoted by ϵ) ranging from 1 to 3.20 exhibited distinctive FIV response regimes and VIV-galloping interactions. Interestingly, as ϵ was increased to 3.2, a significant reduction in the afterbody, the maximum vibration amplitude was observed to be $2.17b$ at the highest reduced velocity tested $U^* = 12$, an increase of over 400% compared to that of a sphere undergoing VIV. Moreover, the $\epsilon = 3.2$ spheroid could reach a maximum time-averaged power coefficient ($\overline{C}_P$) of 0.165, approximately 660% higher than that observed in VIV of spheres.

Although previous studies have indicated the significant effect of the mass and damping ratios on FIV response of bluff bodies (for two-dimensional bodies, e.g. Govardhan and Williamson (2006), Klamo et al. (2006), Soti et al. (2018), Zhao et al. (2019b), Han et al. (2023a), and for three-dimensional spheres, e.g. Govardhan and Williamson (2005)), a notable gap exists in the literature regarding the influence of the mass-damping parameter on the FIV response of oblate spheroids and their FIV energy harvesting implications. In addition to its value for fundamental FIV studies, the oblate spheroid is representative of streamlined bluff bodies encountered in marine and offshore structures and in FIV-based energy-harvesting systems, underscoring the engineering relevance of the present work. Here, mass ratio (m^*) represents the ratio of the total oscillating mass (m) to the mass of the displaced fluid (m_d), namely $m^* = m/m_d$. It has been shown that both the peak vibration amplitude and synchronisation regime in FIV of bluff bodies can be influenced by mass and damping ratios (see Govardhan and Williamson, 1997, 2000; Khalak and Williamson, 1999; Jauvtis et al., 2001). On the other hand, studying the effect of structural damping ratio could shed light on the implied energy harvesting performance from FIV of structures (see Wang et al., 2017; Soti et al., 2018; Lo et al., 2024; Zhao et al., 2022; Lo et al., 2023; Han et al., 2023b,c). Research on FIV energy harvesting can be found in the review articles by Bernitsas et al. (2008), Wang et al. (2020), Lv et al. (2021). To address the existing knowledge gap, the present study aims to provide a comprehensive understanding of how varying mass ratio within the range of $32 \leqslant m^* \leqslant 250$ affects the FIV response of an oblate spheroid of $\epsilon = 2$, a representative spheroid case selected from the previous study of Cordero Obando et al. (2024).

The article is structured into several sections. Section 2 describes the experimental setup, followed by results and discussion in Section 3. Finally, Section 4 draws conclusions from the present study.

2. Experimental methodology

2.1. Fluid–structure system

The fluid–structure system under study is illustrated in Fig. 1 (d). The elastically mounted oblate spheroid (i.e. oscillator) is modelled as a mass-damper-spring system with the governing equation of motion given by

$$m\ddot{y} + c\dot{y} + ky = F_y, \tag{1}$$

where m is the total oscillating mass, c is the structural damping, k is the spring constant, y is the cross-flow body displacement, and F_y is the transverse fluid force.

2.2. Experimental set-up

The experiments were conducted in the *Fluids Laboratory for Aeronautical and Industrial Research (FLAIR)* at Monash University, using a recirculating water channel facility with a test section of 4000 mm in length, 800 mm in depth and 600 mm in width. A low-friction air-bearing rig was utilised to model the hydro-elastic system, which constrained the cylinder model to oscillate transversely to the oncoming water flow. An eddy-current damper mechanism was mounted to the air-bearing rig to accurately adjust the structural damping of the system (see Fig. 1). The flow turbulence level was maintained at less than 1%. Further information on the air-bearing system and the water-channel facility can be found in Zhao et al. (2014).

The oblate spheroid model used is a precision-machined bluff body made of Renshape 460 (medium high-density polyurethane). The model has a streamwise diameter $a = 25 \pm 0.20$ mm referred to as the minor diameter, and a cross-section diameter $b = 50 \pm 0.20$ mm referred to

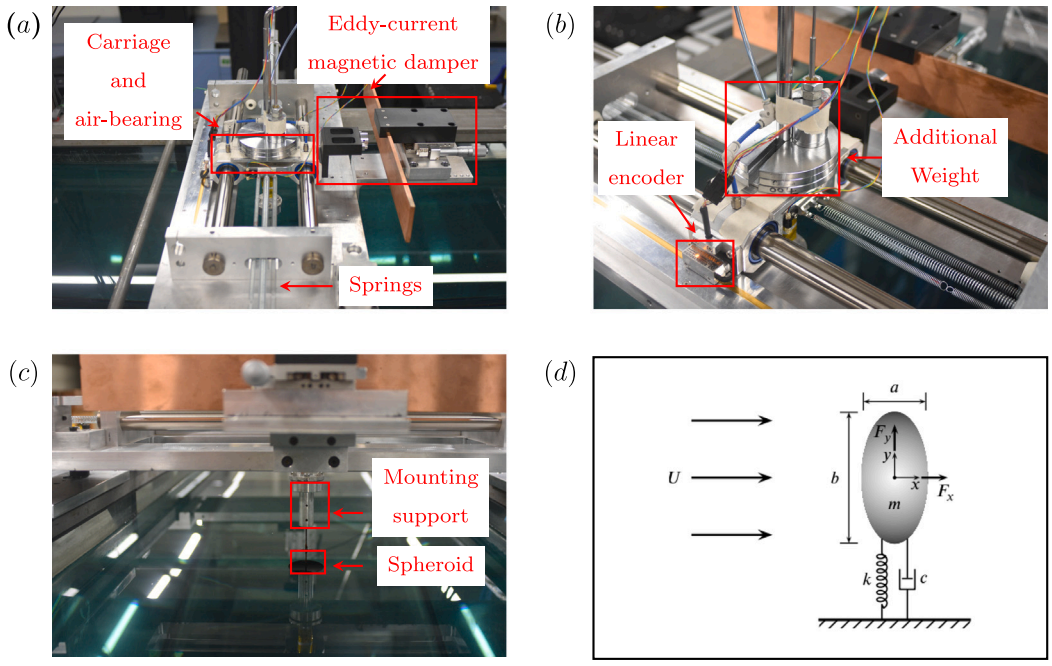


Fig. 1. Photographs showing the experimental set-up, in (*a*) top view, (*b*) side view, and (*c*) back view. Schematic of the oblate spheroid in (*d*), with U being the free-stream velocity, F_x and F_y being the streamwise and transverse forces acting on the body, a being the streamwise diameter, and b being the cross-section diameter.

Table 1
The experimental parameters: total mass (m), displaced fluid mass (m_d), added mass (m_A), added mass coefficient (C_A), the damping ratio (ζ), and the natural frequencies in quiscient air (f_{na}) and water (f_{nw}), for all mass ratios tested.

m^*	m [g]	m_d [g]	m_A	C_A	ζ	f_{na} [Hz]	f_{nw} [Hz]	$(m^*+C_A)\zeta$
32	1040.5	32.6	13.88	0.4260	0.006412	0.692	0.688	0.2074
50	1639.0	32.7	23.98	0.7335	0.004000	0.685	0.680	0.2034
100	3273.4	32.7	30.23	0.9247	0.002030	0.686	0.682	0.2051
150	4906.5	32.7	12.23	0.3741	0.001359	0.689	0.688	0.2044
250	8175.9	32.7	12.49	0.3828	0.000821	0.687	0.687	0.2056

as the major diameter (see Fig. 1). These dimensions give a cross-section aspect ratio of $\epsilon = b/a = 2.00$. The oblate spheroid was supported using a cylindrical support rod of 2.00 mm in diameter, resulting in a diameter ratio between the spheroid and the support rod of 25. The immersion length for the spheroid was approximately $1.1b$. The total oscillating mass associated with the oblate spheroid was $m = 1040.5$ g, and the displaced fluid mass was $m_d = 4\rho\pi a^2 b/3 = 32.7$ g, which results in a minimum achievable mass ratio of $m^* = 32$. The mass ratio was varied within the range of $32 \leqslant m^* \leqslant 250$ by adding supplementary weight to the carriage attached to the air-bearing rig (see Fig. 1). For each tested m^*, the configuration of extension springs on either side of the oscillating mass was adjusted to maintain similar ranges of U^* and Re across all cases. Natural frequencies in quiescent water f_{nw} and air f_{na} were determined through free-decay tests. Detailed parameter values associated with each mass ratio, including fluid added mass $m_A = ((f_{na}/f_{nw})^2 - 1)m$, added mass coefficient $C_A = m_A/m_d$, the damping ratio with consideration of the added mass ($\zeta = c/(2\sqrt{k(m+m_A)})$), among others, are provided in Table 1. Relevant discussions on "added mass" are documented in Govardhan and Williamson (2000) and Limacher (2021).

2.3. Data acquisition and processing methods

The data acquisition was made using a workstation computer equipped with LabVIEW (National Instruments, USA) and a USB data acquisition device (model: USB6218-BNC, National Instruments, USA). This computer allowed the control of flow velocity. The structural displacement was measured using a non-contact digital optical linear encoder (model: RGH24, Renishaw, UK) that was installed on the air-bearing rig (see Fig. 1). This linear encoder has a measurement range of ±200 mm, with an accuracy of 1 μm. The recorded displacement was used to calculate the transverse fluid force (F_y) (see Zhao et al., 2018b). The data acquisition was sampled at 100 Hz for more than 60 vibration cycles for each reduced velocity. The reduced velocity range tested was $3 \leqslant U^* \leqslant 12$, and the corresponding Reynolds number range was $5000 \leqslant Re = Ub/\nu \leqslant 20\,000$, with ν being the kinematic viscosity of the water.

3. Results and discussion

3.1. FIV response regimes

Fig. 2 shows the normalised amplitude response (A^*_{10}) and the normalised power spectral density (PSD) contours for the body vibration frequency ($f^*_y = f_y/f_{nw}$) as functions of the reduced velocity (U^*) for various mass ratios. Furthermore, Fig. 3 shows the transverse fluid force frequency response ($f^*_{C_y} = f_{C_y}/f_{nw}$), illustrating different FIV regimes. Note that A^*_{10} denotes the mean of the top 10% vibration amplitudes measured for each reduced velocity. These figures cover both increasing and decreasing U^* trends.

The PSD contour plots on a logarithmic scale for the fluid force coefficient were generated by applying a Fast Fourier Transform to the time series at each U^* value, normalising the resulting spectra by their maximum energy, and sequentially stacking each spectrum (for details,

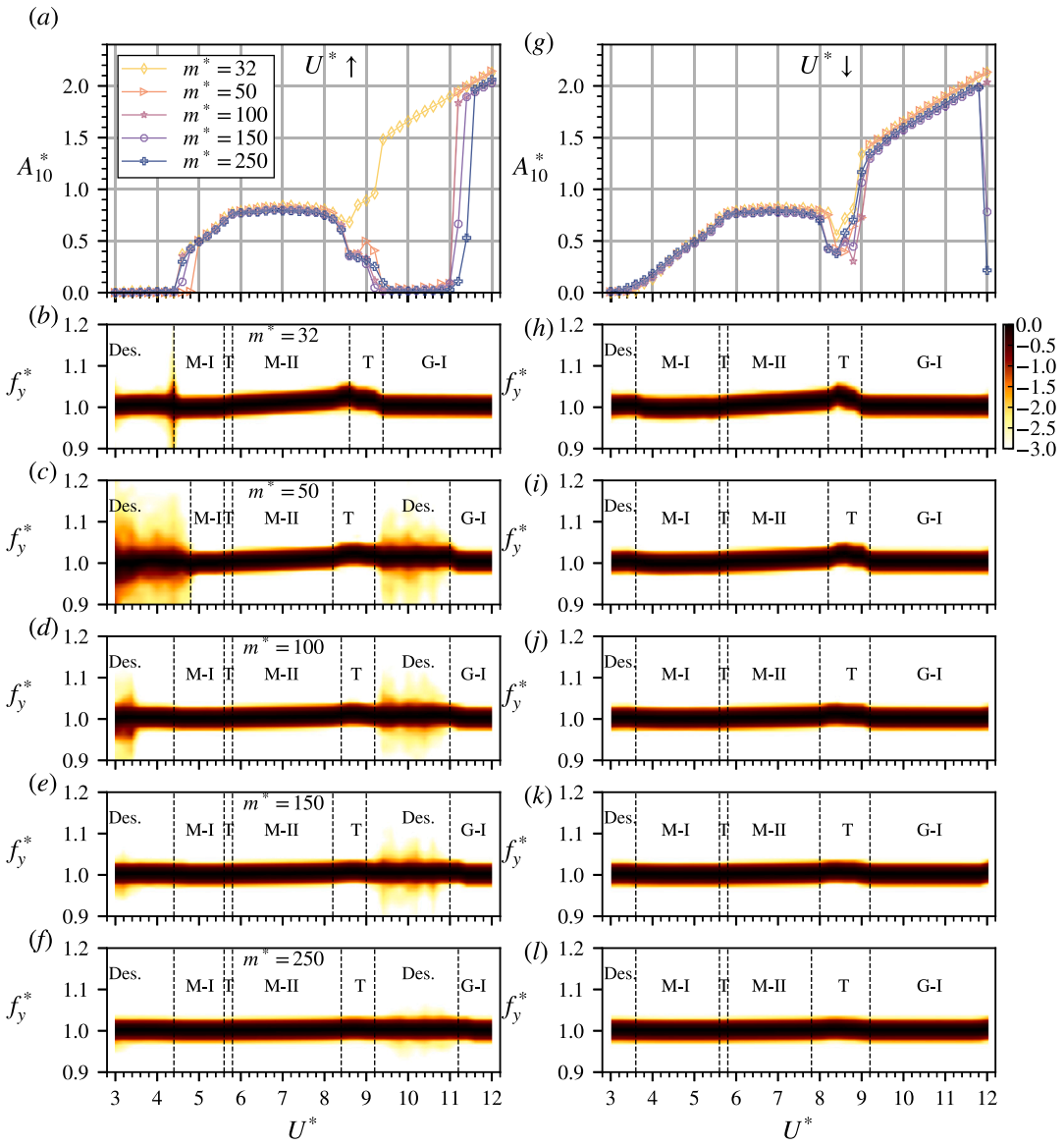


Fig. 2. Amplitude response (A_{10}^*) along with the power-spectral density (PSD) contours of the oblate spheroid displacement frequency (f_y^*) as a function of increasing reduced velocity ($U^* \uparrow$) in ($a - f$) and decreasing reduced velocity ($U^* \downarrow$) in ($g - l$) for various mass ratios. Note the following abbreviations: Mode I regime (M-I), Mode II regime (M-II), Transition regime (T), and galloping-like regime (G-I).

see Zhao et al., 2014). This method allows the frequency components with their relative strengths to be visualised as a function of U^*.

Fig. 4 presents the root-mean-square (rms) of the transverse fluid force (lift) coefficient, denoted as $C_y^{rms} = F_y/(\frac{1}{8}\rho U^2 \pi b^2)$, along with its relative phase to the body displacement (y), namely the total phase (ϕ_t). Additionally, Fig. 5 depicts the rms coefficient of the vortex force, denoted as $C_v^{rms} = F_v/(\frac{1}{8}\rho U^2 \pi b^2)$, and its relative phase to the body displacement, namely the vortex phase (ϕ_v). The determination of the vortex force follows the methods by Lighthill (1986) and Govardhan and Williamson (2000).

Fig. 6 illustrates how the periodicity varies with U^* across different mass ratio values. According to the analysis by Jauvtis et al. (2001), the periodicity of a signal can be quantified using the definition $P = \sqrt{2} y_{rms}/y_{max}$.

As shown in Figs. 2 and 3, the A_{10}^* and frequency responses for the mass ratio cases of $50 \leqslant m^* \leqslant 250$ appear to be highly similar, while the tested lowest mass ratio case of $m^* = 32$ displays a slightly different response. Nonetheless, the amplitude response is classified into three distinct "lock-in" regimes across the mass ratios for both increasing and decreasing increments of U^*. To facilitate the dynamic response analysis, the $m^* = 32$ case will be examined in detail for increasing U^* values. Note that the following analysis can be applied to the other m^* cases in order to determine the boundaries of distinct FIV regimes.

The first regime, referred to as Mode I, is characterised by a nearly linear increase in A_{10}^* within the range of $4.4 \leqslant U^* \leqslant 5.6$. The onset of Mode I is marked by a sudden increase in both C_y^{rms} and C_v^{rms} at $U^* = 4.4$ (see Figs. 4 and 5). Within this regime, C_y^{rms} reaches a peak value of 0.37 at $U^* = 5.6$, corresponding to the highest vibration amplitude observed. In contrast, ϕ_t remains relatively stable at approximately 25° throughout Mode I. This regime spans a reduced velocity range of $4.4 \leqslant U^* \leqslant 5.8$, where a clear wake-body synchronisation is evident, with dominant frequencies of f_y and f_{C_y} aligning at f_{nw} (see Figs. 2 and 3). Mode I is thus identified as a VIV-dominated region with high periodicity (see Fig. 6).

Fig. 7 presents sample time traces of the normalised body displacement (y^*) and fluid forces (C_y and C_v) over normalised time $\tau = t f_{nw}$. The displacement and forces exhibit a clearly periodic, sinusoidal-like variation. The frequency response reveals a dominant component at

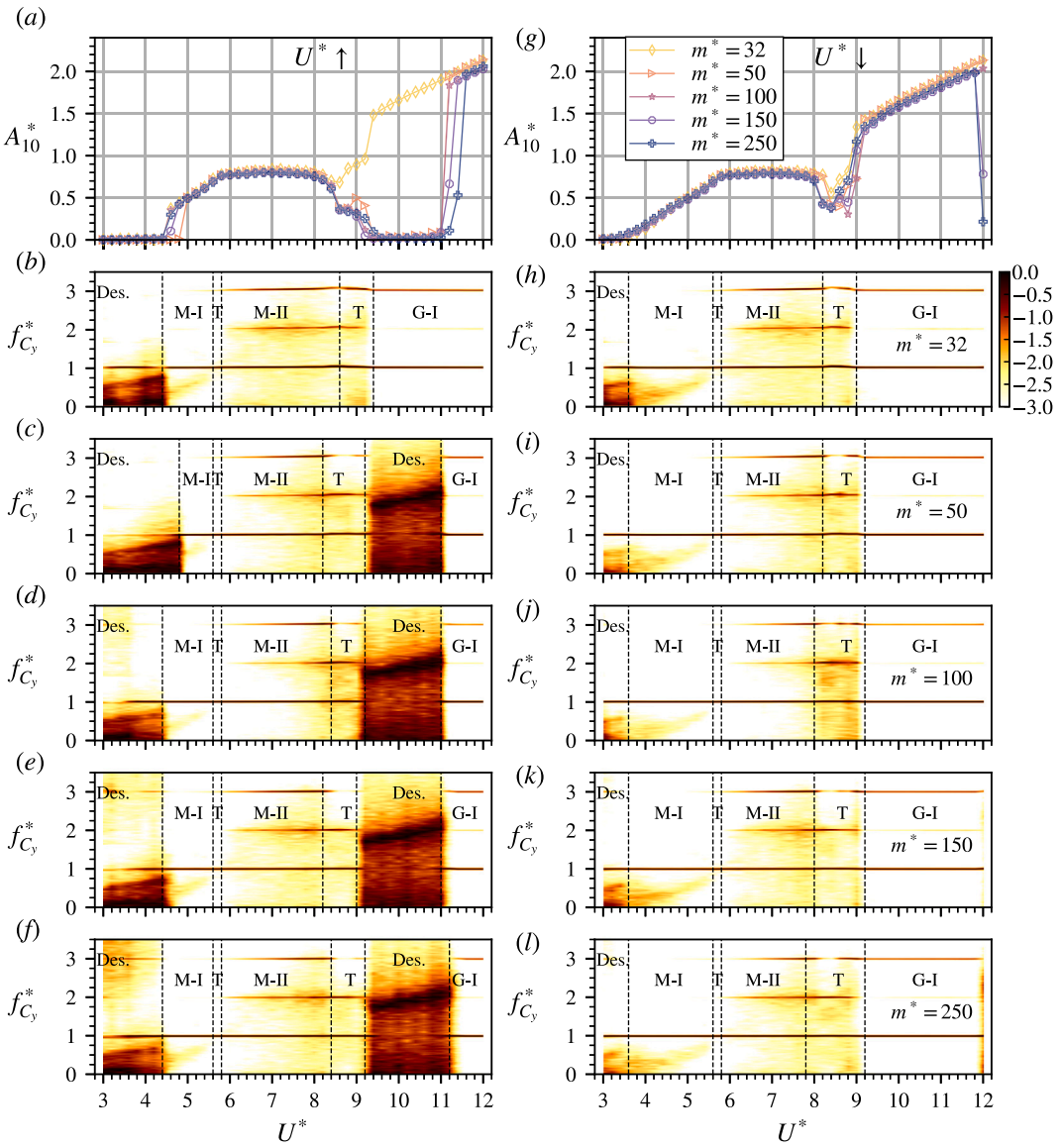


Fig. 3. A^*_{10} response along with the PSD contours of the total transverse fluid force frequency ($f^*_{C_y}$) as a function of increasing reduced velocity ($U^* \uparrow$) in $(a-f)$ and decreasing reduced velocity ($U^* \downarrow$) in $(g-l)$ for various mass ratios. Note the following abbreviations: Mode I regime (M-I), Mode II regime (M-II), Transition regime (T), and galloping-like regime (G-I).

$f^* = 1$ and a much weaker harmonic component at $f^* = 3$, although the latter is not evident in the frequency contour plots. In this case, the reduced velocity corresponding to these plots is $U^* = 5.6$, within the Mode I regime.

As the reduced velocity is further increased, a second regime termed Mode II, emerges over $5.8 \leqslant U^* \leqslant 8.6$, which is characterised by a plateau trend of the A^*_{10} response (see Fig. 3). The body vibration is self-limited during this regime, with a saturation peak amplitude of approximately $0.7b$. Here, ${C_y}^{rms}$ shows a gradual decrease, whereas ϕ_t continuously increases from 25° to 150°, and ϕ_v from 50° to 160°. Interestingly, ${C_v}^{rms}$ remains almost constant at 0.20 over the entire regime (see Fig. 4 and 5). In this regime, a weak second harmonic ($f^*_{C_y} \sim 2$) and a third harmonic ($f^*_{C_y} \sim 3$) are observed (see Fig. 3), with Mode II exhibiting highly periodic oscillations (see Fig. 6).

Fig. 8 presents sample time traces of y^*, C_y and C_v, along with their frequency PSD plots, for all mass ratio cases at $U^* = 7.2$. In all cases, the body displacement exhibits a periodic sinusoidal pattern, and its frequency response confirms the dominant frequency component at $f^* = 1$ (i.e. corresponding to the natural frequency f_{nw}). Regarding the fluid forces, their time traces reveal two distinct peaks, as reflected by components at $f^* = 1$ and $f^* = 3$ in the frequency response and with only a minimal contribution at $f^* = 2$. Overall, Mode II is characterised by a strong presence of both the first and third harmonic components in the fluid forces, alongside pronounced periodic sinusoidal body oscillations.

Fig. 9 presents sample time traces of y^*, C_y and C_v, along with their corresponding PSD contour plots at $U^* = 10.2$ for all tested mass ratios; specifically, Fig. 9(a) shows the Mode G-I regime for $m^* = 32$ and Figs. 9$(b-e)$ display the transition regime T for $m^* \geq 50$. For $m^* = 32$, the body displacement exhibits a periodic variation, aligning well with the expected periodicity as seen in Fig. 6. Additionally, the time traces of the fluid forces reveal a secondary peak, indicating the presence of two harmonics in the frequency response. In contrast, for other values of $m^* \geq 50$, the displacement time traces appear non-periodic and highly irregular, suggesting a loss of synchronisation between the vortex shedding frequency and the displacement frequency. This desynchronisation leads to a significant reduction in vibration amplitude. Furthermore, for $m^* \geqslant 50$, the fluid forces appear to be non-periodic and noisy, corresponding to the absence of distinct peaks in their frequency responses.

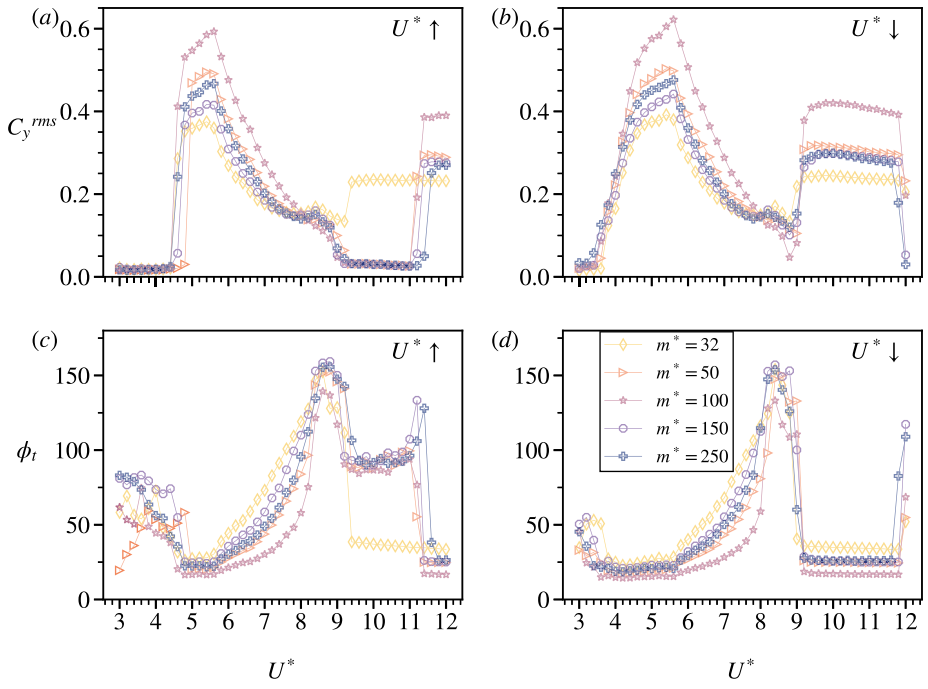


Fig. 4. Variations of the lift force coefficient (C_y^{rms}) and the total phase (ϕ_t) as a function of increasing reduced velocity ($U^*\uparrow$) in (a,c) and decreasing reduced velocity ($U^*\downarrow$) in (b,d) for various mass ratios.

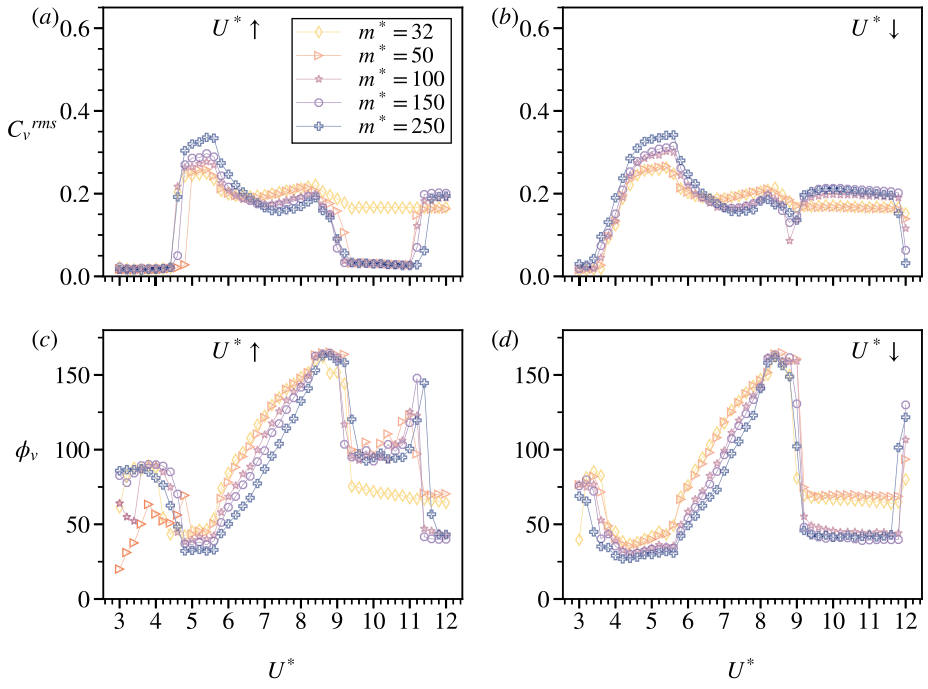


Fig. 5. Variations of the vortex force coefficient (C_v^{rms}) and the vortex phase (ϕ_v) as a function of increasing reduced velocity ($U^*\uparrow$) in (a,c) and decreasing reduced velocity ($U^*\downarrow$) in (b,d) for various mass ratios.

A third vibration regime, designated as Mode G-I, is observed for $U^*\geqslant 9.4$, for the case $m^*=32$. The transition from Mode II to Mode G-I is indicated by a notable increase in A_{10}^* and a significant change in the total and vortex phases within the reduced velocity range of $9.2\leqslant U^*\leqslant 9.4$. Specifically, ϕ_t decreases from 110° to 40°, while ϕ_v drops from 140° to 75° (see Figs. 4 and 5). In the Mode G-I regime, a galloping-like response is observed, characterised by an approximately linear increase in amplitude with flow speed. Within this regime, although there are notable frequency contributions at $f_{C_y}^*\approx 1$ and $f_{C_y}^*\approx 3$, the dominant frequency component is at $f_{C_y}^*\approx 1$. Within the range $9.4\leq U^*\leq 12.0$, the fluid force coefficient, $f_{C_y}^*$, exhibits a strong third-harmonic contribution, suggesting that the large vibration amplitude is linked to this harmonic contribution. Previous studies on transverse and in-line FIVs of bluff bodies (see Zhao et al., 2014, 2018a,c; Wang et al., 2017; Bourguet and Lo Jacono, 2015; Zhao et al., 2018b) have similarly attributed large-amplitude responses to harmonic synchronisations. Mode G-I exhibits a slightly higher oscillation periodicity compared to the VIV-dominated regimes, as shown in Fig. 6.

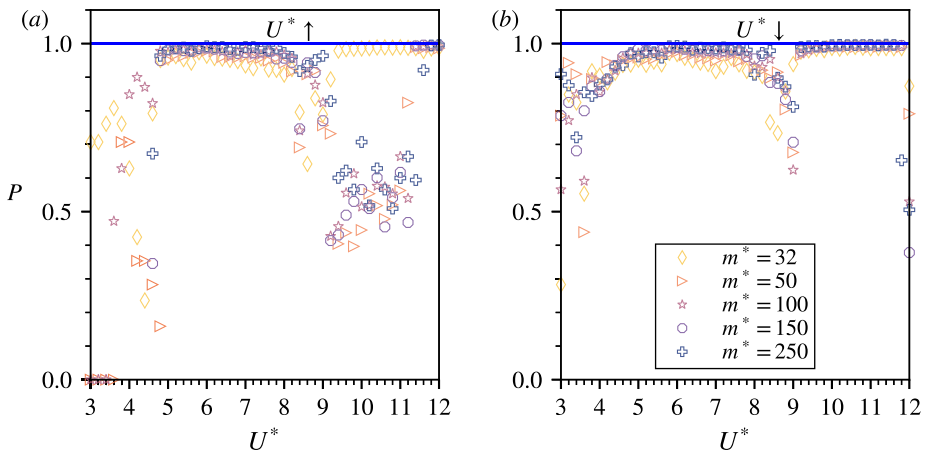


Fig. 6. Periodicity of the spheroid displacement as a function of U^*. The solid blue line represents a purely sinusoidal signal.

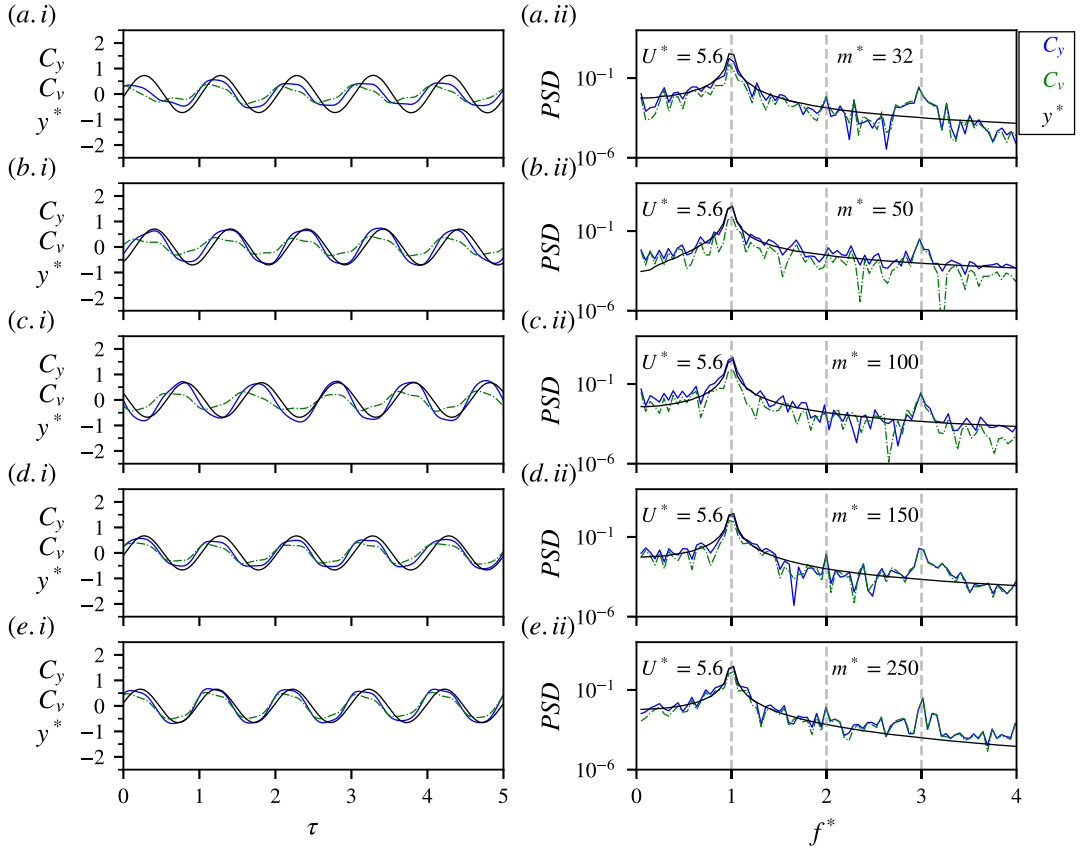


Fig. 7. Sample time traces of the body displacement (y^*), and the coefficients of the total transverse force (C_y) and the vortex force (C_v) at $U^*=5.6$ within the Mode-I regime, along with the corresponding frequency PSD plots for (*a*) $m^*=32$, (*b*) $m^*=50$, (*c*) $m^*=100$, (*d*) $m^*=150$, and (*d*) $m^*=250$. Note that these results correspond to increasing U^* values.

Fig. 10 shows sample time traces of the body displacement and the fluid forces as representative cases from the Mode G-I regime. In this vibration regime, the displacement time traces again exhibit a highly periodic motion, similar to those observed in Mode I and Mode II regimes. However, the time traces of the fluid forces differ significantly from those in Mode II. In this case, the time traces display three distinct peaks per period, with only a minor contribution from the second harmonic ($f^*=2$), as evident in the frequency plots. Notably, the dominant contributions arise from the first and third harmonics, which exhibit almost equal power. This characteristic is a key feature for categorising this galloping-like regime.

In conclusion, within the VIV-dominated regions (Mode-I and Mode-II), the A^*_{10} amplitude response remains consistent across all tested mass ratios. However, the mass ratio significantly influences the transition between the VIV-dominated regime and the galloping-like regime. For instance, the end of the VIV-dominated (i.e. end of Mode II) for $m^*=32$ is marked by a transition branch, referred to as T, followed by a continuous transition towards a galloping-like regime. This case is categorised as *hard galloping* (see Naudascher and Rockwell, 2005), where the galloping-like response requires an externally imposed initial threshold amplitude. Conversely, for $m^*\geqslant 50$, the end of the Mode II regime is marked by the presence of a transition regime T, followed by a desynchronisation regime where the amplitude of the response

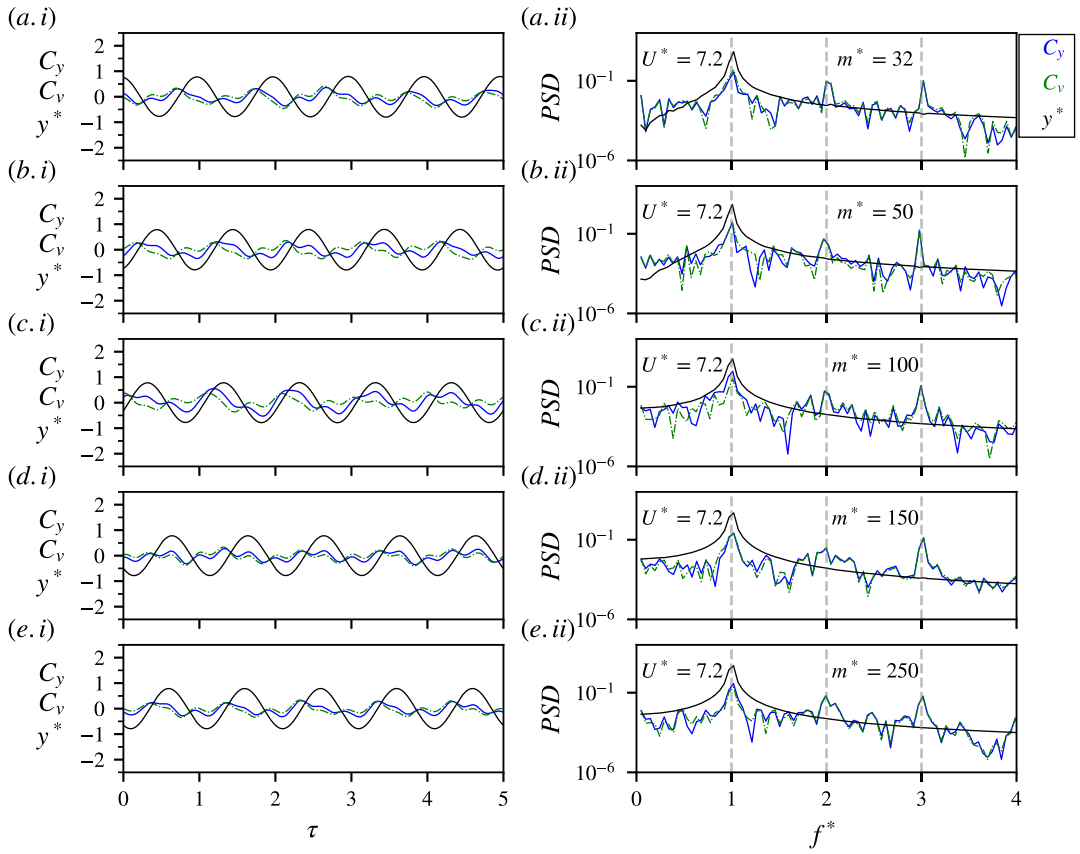


Fig. 8. Sample time traces of the body displacement (y^*), and the coefficients of the total transverse force (C_y) and the vortex force (C_v) at $U^* = 7.2$ within the Mode-II regime, along with the corresponding frequency PSD plots for (*a*) $m^* = 32$, (*b*) $m^* = 50$, (*c*) $m^* = 100$, (*d*) $m^* = 150$, and (*d*) $m^* = 250$. Note that these results correspond to increasing U^* values.

is considerably suppressed before the galloping-like response builds up spontaneously from rest at even higher U^* values. Hence, this galloping-like response is categorised as *soft galloping* (see Naudascher and Rockwell, 2005), which can occur without a hard trigger/kick-off. Interestingly, within the galloping-like regime, there is a slight decrease in vibration amplitude caused by an increase in m^* while maintaining a saturation peak amplitude close to $2b$ for all the m^* tested. Moreover, the onset of the galloping-like regime is of particular interest, which is equal to $U^* = 9.4$ for $m^* = 32$, whereas a higher reduced velocity of $U^* = 11.0$ is required for the other tested cases of $m^* \geqslant 50$.

3.2. Hysteresis effects in the amplitude response

Several significant characteristics emerge when examining the impact of altering the direction of U^* increments on the amplitude response and FIV regimes. Across the evaluated U^* range, the A^*_{10} response consistently exhibits a three-branch pattern (i.e. Modes I, II, and G-I), independent of the U^* increment direction for the case of $m^* = 32$. Additionally, it is important to note that the saturation peak amplitude remains unaffected. However, there is a variation in the U^* ranges corresponding to the lock-in regimes. Notably, the initiation of the VIV-dominated region (i.e. the transition between desynchronisation and Mode I) occurs at different U^* values. For increasing U^* increments, the Mode I regime begins at $U^* = 4.4$, whereas for decreasing increments, it starts at $U^* = 3.4$. Compared to the other two vortex formation modes, Mode I regime appears to be influenced by the initial state of the oblate spheroid system, particularly the oscillation amplitude. This dependency elucidates why the U^* increment direction determines whether a synchronised (e.g. Mode I) or desynchronised response is observed for lower reduced velocities ($3.4 \leqslant U^* \leqslant 4.4$). As the Mode I regime is VIV-dominated, the hysteresis behaviour likely stems from the effect of transverse oscillations on the wake structure formed behind the spheroid, similar to the observations of Blevins (1990). Similar amplitude-dependent hysteresis near the onset of lock-in (e.g. Mode I in the current study) has been reported for vibrating spheres (Provansal et al., 2003; Behara et al., 2011) and circular cylinders (Williamson and Govardhan, 2004; Singh and Mittal, 2005). In addition, for $m^* \geqslant 50$, it can be observed that for a decreasing increment of U^*, the desynchronisation region between the VIV-dominated regime and the galloping-like regime displayed in the increasing increment of U^* disappears and gives place to a transition regime of the non-periodic oscillations.

3.3. FIV energy harvesting from the spheroid

This subsection presents the potential energy harvesting performance from FIV of the spheroid. The instantaneous power is given by $P = F_y \cdot \dot{y}$, and its non-dimensional coefficient is as defined by

$$C_P = \frac{P}{\frac{1}{2}\rho U^3 \pi (b^2/4)} = \frac{F_y \cdot \dot{y}}{\frac{1}{2}\rho U^3 \pi (b^2/4)}. \tag{2}$$

In the present study, the implied FIV energy harvesting performance is evaluated by the time-average power coefficient, as expressed by Zhao et al. (see 2022) by

$$\overline{C}_P = \frac{1}{t}\int_0^t C_P(t)\,\mathrm{d}t. \tag{3}$$

Fig. 11 shows the time-average power coefficient as a function of the reduced velocity (U^*) for various mass ratios. Two distinct scenarios are presented: in Fig. 11(*a*), the reduced velocity is varied in an increasing trend, while in Fig. 11(*b*), the reduced velocity is varied in a decreasing trend. Notably, across all tested mass ratios, the variation in the output

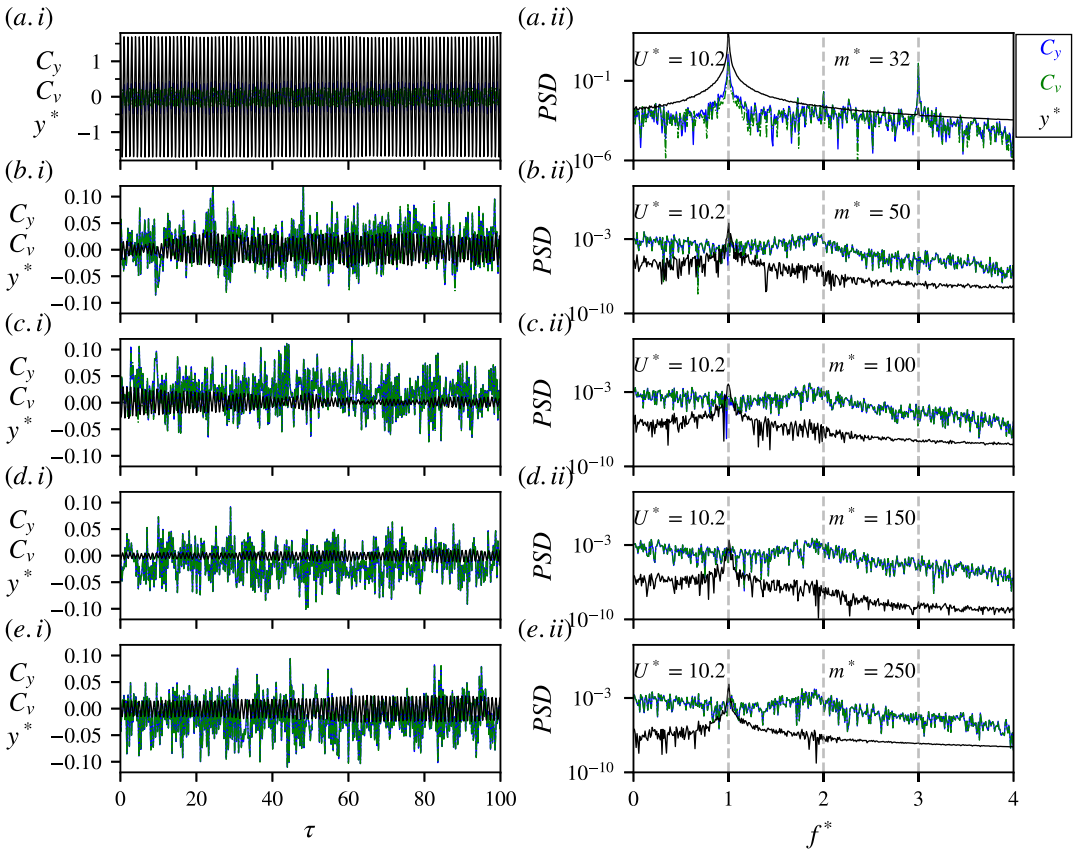


Fig. 9. Sample time traces of the body displacement (y^*), and the coefficients of the total transverse force (C_y) and the vortex force (C_v) at $U^* = 10.2$ within the Mode G-I regime, along with the corresponding frequency PSD plots for (*a*) $m^* = 32$, and within the desynchronisation region for (*b*) $m^* = 50$, (*c*) $m^* = 100$, (*d*) $m^* = 150$, and (*d*) $m^* = 250$. Note that these results correspond to increasing U^* values.

power coefficient remains nearly the same throughout the VIV region, irrespective of the direction of the change in the reduced velocity.

Fig. 12 shows that for all the tested cases having a mass-damping parameter $(m^* + C_A)\zeta$ close to 0.20, the maximum output power coefficient is observed to be $\overline{C}_P \approx 0.10$, occurring at $U^* \approx 5.8$ within the VIV region. However, depending on the direction of change of the reduced velocity, $\overline{C}_P$ varies, particularly in the galloping-like region. It is also noteworthy that in the galloping-like response regime, $\overline{C}_P$ appears to stable, making it more suitable for practical applications, despite being lower than the maximum $\overline{C}_P$ reached in the VIV regimes. However, by systematically varying the damping ratio, one can identify an optimum range that maximises energy extraction while maintaining dynamic stability. This approach has been successfully demonstrated for circular cylinders (Soti et al., 2017; Zhao et al., 2022) and could be applied to this case with the aim of increasing the value of $\overline{C}_P$.

4. Conclusions

Extensive experiments have been conducted to investigate the impact of the mass-damping parameter $(m^* + C_A)\zeta$ on the flow-induced vibration (FIV) response of an oblate spheroid with an aspect ratio of $\epsilon = 2.00$. Five distinct mass ratio values, $m^* = [32, 50, 100, 150, 250]$, were tested while keeping a constant value of $(m^* + C_A)\zeta \sim 0.20$ within a reduced velocity range of $3.0 \leqslant U^* \leqslant 12.0$ (equivalent to $5000 \lesssim Re \lesssim 20\,000$).

All m^* cases exhibited a dynamic response characterised by both vortex-induced vibration (VIV) and galloping-like vibration regions. It was observed that with increasing mass ratio, there was a slight decrease in vibration amplitude, particularly in the galloping-like region, while the VIV-dominated regime showed minimal change in vibration amplitude. For $m^* = 32$, there is a smooth transition between the VIV and galloping-like regimes, whereas, for $m^* \geq 50$, a desynchronisation region appears to separate both FIV phenomena. This latter result implies that depending on the value of m^*, there are two types of galloping-like response: a hard galloping-like response for $m^* = 32$ and a soft galloping-like response for $m^* > 32$. Overall, it was found that while keeping $(m^* + C_A)\zeta$ almost constant over a wide range of m^*, the amplitude of response remains almost unchanged over the range of U^* tested.

Future work should explore FIV responses of the spheroid at lower values of the mass-damping parameter. This would determine whether the FIV continues to exhibit a three-branch response or if additional influences on the FIV emerges. Additionally, flow visualisation techniques such as PIV would be highly beneficial for correlating wake structure with the observed response regimes. Cordero Obando et al. (2024) previously employed planar PIV to investigate the FIV response of elastically mounted oblate spheroids of different aspect ratios (ϵ); however, those measurements were restricted to the horizontal mid-plane and therefore did not capture the three-dimensional structure of the wake. A natural next step would be to extend these studies by conducting tomographic PIV or wake reconstruction from multiple vertical planes.

Furthermore, system identification techniques such as sparse identification of nonlinear dynamics (SINDy) (Brunton et al., 2016) could be used to extract reduced-order models of the nonlinear wake dynamics and to better capture the transitions between response modes (Brunton et al., 2020; Mendez et al., 2023; Marra et al., 2024). Extending such approaches to the present study would be a valuable complement to current experimental observations, providing a framework for predictive modelling of complex FIV responses.

Note that in potential practical applications, environmental variability could alter the FIV response and, in turn, the energy harvesting

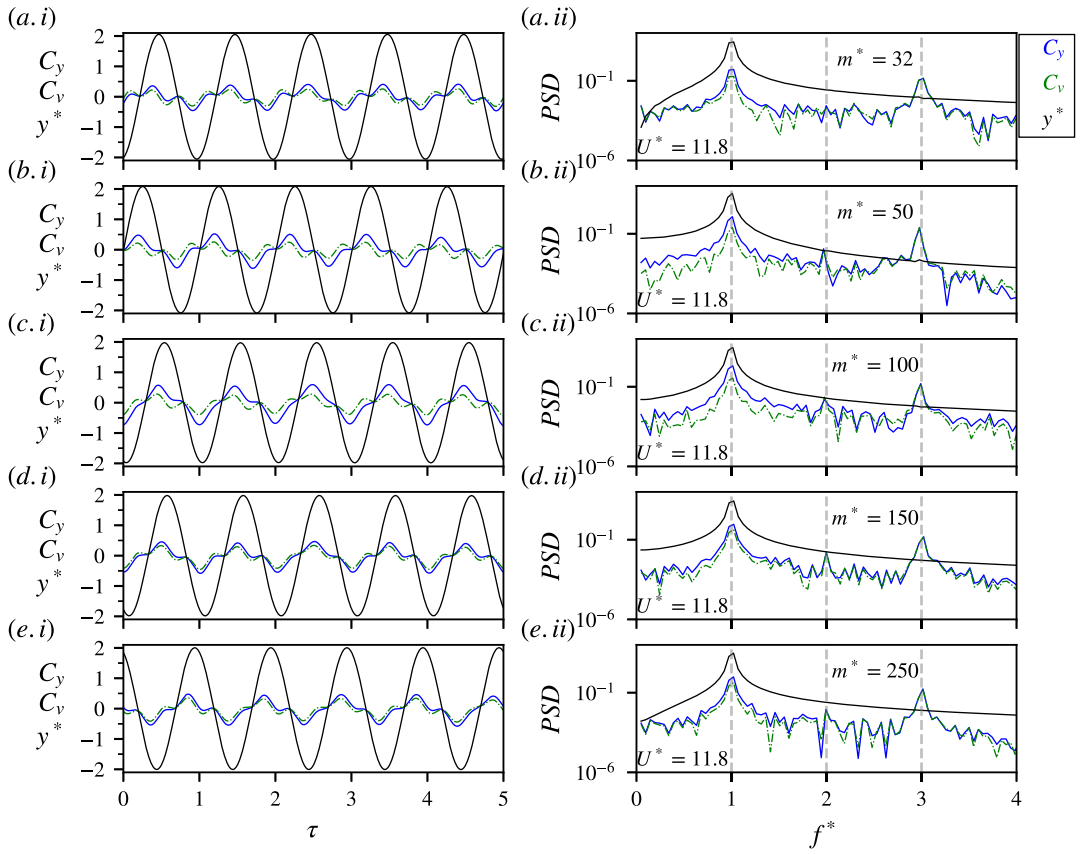


Fig. 10. Sample time traces of the body displacement (y^*), and the coefficients of the total transverse force (C_y) and the vortex force (C_v) at $U^* = 11.8$ within the Mode G-I regime, along with the corresponding frequency PSD plots for (*a*) $m^* = 32$, (*b*) $m^* = 50$, (*c*) $m^* = 100$, and (*d*) $m^* = 150$, (*d*) $m^* = 250$. Note that these results correspond to increasing U^* values.

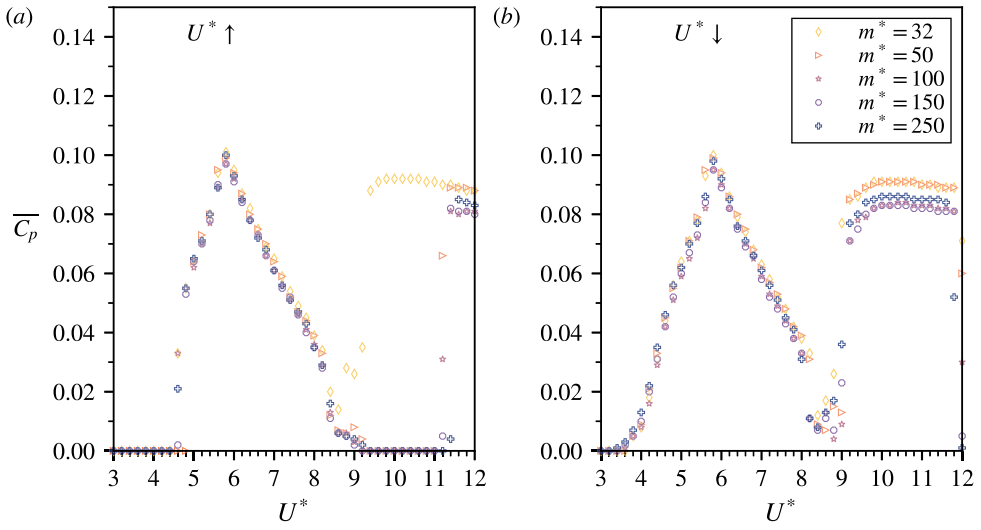


Fig. 11. Variation of time-average power coefficient, $\overline{C}_p$, as a function of (*a*) increasing reduced velocity ($U^* \uparrow$) and (*b*) decreasing reduced velocity ($U^* \downarrow$), for various mass ratios.

performance. In this set of experiments, the turbulence level in the water channel was approximately 1%. The present study is constrained by (i) a Reynolds-number range $5000 \lesssim < Re \lesssim 20\,000$, set by the available facility speed and model scale, and (ii) the achievable mass-ratio window, $32 \leq m^* \leq 250$, imposed by the air-bearing rig's baseline mass and payload capacity. Consequently, our conclusions are most directly applicable within this parameter space. To better understand scaling to real-world conditions, future work should involve experiments under higher turbulence intensities and higher Reynolds numbers (Lu et al., 2020; Razaviyn et al., 2025; de Oliveira et al., 2025; Wang et al., 2025), as well as across a broader range of m^* values to assess the influence on VIV and galloping-like responses, and to identify the scales at which such spheroidal geometries may function as effective FIV-based energy harvesters.

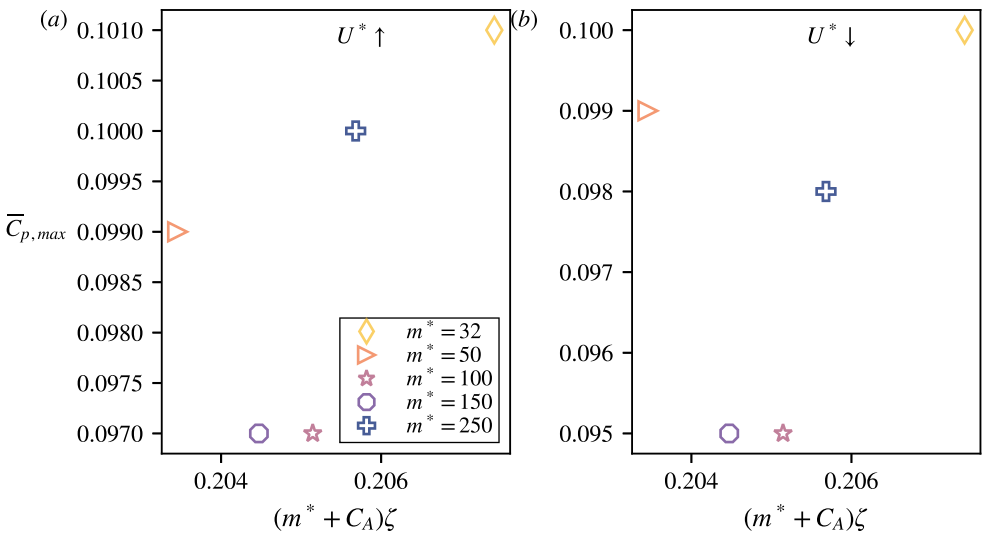


Fig. 12. Variation of the maximum power coefficient, $\overline{C}_{p\,max}$, as a function of the mass-damping parameter, $(m^* + C_A)\zeta$, for (*a*) increasing reduced velocity ($U^* \uparrow$) and (*b*) decreasing reduced velocity ($U^* \downarrow$).

CRediT authorship contribution statement

Adrian Cordero Obando: Writing – review & editing, Writing – original draft, Project administration, Methodology, Investigation, Formal analysis, Data curation, Conceptualization. **Kerry Hourigan:** Writing – review & editing, Supervision, Funding acquisition, Formal analysis. **Mark C. Thompson:** Writing – review & editing, Supervision, Funding acquisition, Formal analysis. **Jisheng Zhao:** Writing – review & editing, Supervision, Funding acquisition, Formal analysis, Conceptualization.

Declaration of competing interest

The authors declare that they have no known competing financial interests or personal relationships that could have appeared to influence the work reported in this paper.

Acknowledgements

This work was supported by the Australian Research Council through the Discovery Early Career Research Award DE200101650 (J.Z.) and the Discovery Project grant DP210100990.

Data availability

Data will be made available on request.

References

Bearman, P.W., Gartshore, I.S., Maull, D., Parkinson, G.V., 1987. Experiments on flow-induced vibration of a square-section cylinder. J. Fluids Struct. 1 (1), 19–34.
Behara, S., Borazjani, I., Sotiropoulos, F., 2011. Vortex-induced vibrations of an elastically mounted sphere with three degrees of freedom at Re = 300: hysteresis and vortex shedding modes. J. Fluid Mech. 686, 426–450.
Bernitsas, M.M., Raghavan, K., Ben-Simon, Y., Garcia, E., 2008. VIVACE (Vortex Induced Vibration Aquatic Clean Energy): A new concept in generation of clean and renewable energy from fluid flow. J. Offshore Mech. Arct. Eng. 130 (4).
Blevins, R.D., 1990. Flow-Induced Vibration. Krieger Publishing Company, Florida.
Bourguet, R., Lo Jacono, D., 2015. In-line flow-induced vibrations of a rotating cylinder. J. Fluid Mech. 781, 127–165.
Brooks, P.N.H., 1960. Experimental Investigation of the Aeroelastic Instability of Bluff Two-dimensional Cylinders (Masters thesis). University of British Columbia.
Brunton, S.L., Noack, B.R., Koumoutsakos, P., 2020. Machine learning for fluid mechanics. Annu. Rev. Fluid Mech. 52, 477–508.
Brunton, S.L., Proctor, J.L., Kutz, J.N., 2016. Sparse identification of nonlinear dynamics with control (SINDYc). IFAC-PapersOnLine 49 (18), 710–715.
Cordero Obando, A., Thompson, M.C., Hourigan, K., Zhao, J., 2024. Effect of aspect ratio on flow-induced vibration of oblate spheroids and implications for energy generation. J. Fluids Struct. 128, 104137.
de Langre, E., 2006. Frequency lock-in is caused by coupled-mode flutter. J. Fluids Struct. 22 (6), 783–791.
de Oliveira, F.J., Khodaei, Z.S., Buxton, O.R., 2025. The influence of free-stream turbulence on the fluctuating loads experienced by a cylinder exposed to a turbulent cross-flow. J. Fluid Mech. 1011, A47.
Facchinetti, M.L., de Langre, E., Biolley, F., 2004. Coupling of structure and wake oscillators in vortex-induced vibrations. J. Fluids Struct. 19 (2), 123–140.
Govardhan, R., Williamson, C.H.K., 1997. Vortex-induced motions of a tethered sphere. J. Wind Eng. Ind. Aerodyn. 69, 375–385.
Govardhan, R., Williamson, C.H.K., 2000. Modes of vortex formation and frequency response of a freely vibrating cylinder. J. Fluid Mech. 420, 85–130.
Govardhan, R., Williamson, C.H.K., 2005. Vortex-induced vibrations of a sphere. J. Fluid Mech. 531, 11–47.
Govardhan, R., Williamson, C.H.K., 2006. Defining the 'modified Griffin plot' in vortex-induced vibration: revealing the effect of Reynolds number using controlled damping. J. Fluid Mech. 561, 147–180.
Gupta, S., Lo, J.C., Zhao, J., Thompson, M.C., Hourigan, K., 2025. The role of an afterbody in flow-induced vibration of cylinders at low to moderate Reynolds numbers. J. Fluid Mech. 1007, A6.
Han, P., De Langre, E., Thompson, M.C., Hourigan, K., Zhao, J., 2023a. Vortex-induced vibration forever even with high structural damping. J. Fluid Mech. 962, A13.
Han, P., Huang, Q., Pan, G., Qin, D., Wang, W., Gonçalves, R.T., Zhao, J., 2023b. Optimal energy harvesting efficiency from vortex-induced vibration of a circular cylinder. Ocean Eng. 282, 114869.
Han, P., Huang, W.-X., Qin, D., Wang, J., Zhao, J., 2023c. An analytical model for estimating the maximum energy harvesting efficiency from vortex-induced vibration. J. Fluids Struct. 122, 103961.
Hourigan, K., Zhao, J., Leweke, T., Thompson, M.C., 2026. Flow-induced vibration of bluff bodies. In: Volume 5: Nonlinear Dynamics and Vibrations: Applications in Engineering, Editor G. Rega. World Scientific, (in press).
Jauvtis, N., Govardhan, R., Williamson, C.H.K., 2001. Multiple modes of vortex-induced vibration of a sphere. J. Fluids Struct. 15 (3), 555–563.
Khalak, A., Williamson, C.H.K., 1999. Motions, forces and mode transitions in vortex-induced vibrations at low mass-damping. J. Fluids Struct. 13 (7–8), 813–851.
Klamo, J., Leonard, A., Roshko, A., 2006. The effects of damping on the amplitude and frequency response of a freely vibrating cylinder in cross-flow. J. Fluids Struct. 22 (6–7), 845–856.
Leontini, J.S., Griffith, M., Lo Jacono, D., Sheridan, J., 2018. The flow-induced vibration of an elliptical cross-section at varying angles of attack. J. Fluids Struct. 78, 356–373.
Lighthill, J., 1986. Fundamentals concerning wave loading on offshore structures. J. Fluid Mech. 173, 667–681.
Limacher, E.J., 2021. Added-mass force on elliptic airfoils. J. Fluid Mech. 926, R2.
Lo, J.C., Hourigan, K., Thompson, M.C., Zhao, J., 2023. The effect of structural damping on flow-induced vibration of a thin elliptical cylinder. J. Fluid Mech. 974, A5.
Lo, J.C., Thompson, M.C., Hourigan, K., Zhao, J., 2024. Order of magnitude increase in power from flow-induced vibrations. Renew. Sustain. Energy Rev. 205, 114843.

Lu, Z., Wong, C., Zhou, Y., 2020. Turbulence intensity effect on the axial-flow-induced vibration of an elastic cylinder. J. Fluids Struct. 99, 103144.
Lv, Y., Sun, L., Bernitsas, M.M., Sun, H., 2021. A comprehensive review of nonlinear oscillators in hydrokinetic energy harnessing using flow-induced vibrations. Renew. Sustain. Energy Rev. 150, 111388.
Marra, L., Meilán-Vila, A., Discetti, S., 2024. Self-tuning model predictive control for wake flows. J. Fluid Mech. 983, A26.
McQueen, T., Zhao, J., Sheridan, J., Thompson, M.C., 2021. Vibration reduction of a sphere through shear-layer control. J. Fluids Struct. 105, 103325.
Mendez, M.A., Ianiro, A., Noack, B.R., Brunton, S.L., 2023. Data-driven fluid mechanics: combining first principles and machine learning. Cambridge University Press.
Naudascher, E., Rockwell, D., 2005. Flow-Induced Vibrations: An Engineering Guide. Dover Publications.
Nemes, A., Zhao, J., Lo Jacono, D., Sheridan, J., 2012. The interaction between flow-induced vibration mechanisms of a square cylinder with varying angles of attack. J. Fluid Mech. 710, 102–130.
Païdoussis, M., Price, S., De Langre, E., 2010. Fluid-Structure Interactions: Cross-Flow-Induced Instabilities. Cambridge University Press.
Parkinson, G., 1989. Phenomena and modelling of flow-induced vibrations of bluff bodies. Prog. Aerosp. Sci. 26 (2), 169–224.
Provansal, M., Leweke, T., Schouveiler, L., Guébert, N., 2003. 3D oscillations and vortex-induced vibrations of a tethered sphere in a flow parallel to the thread. In: Proceedings of PSFVIP-4, Chamonix, France. vol. 35.
Razaviyn, Z., Heidari, M., Thangavel, S., Verma, V., Kumar, A., Yadav, A.K., 2025. Marine energy harvesting from fluid flow via vortex induced vibrations. Int. J. Thermofluids 25, 101015.
Sareen, A., Zhao, J., Lo Jacono, D., Sheridan, J., Hourigan, K., Thompson, M.C., 2018a. Vortex-induced vibration of a rotating sphere. J. Fluid Mech. 837, 258–292.
Sareen, A., Zhao, J., Sheridan, J., Hourigan, K., Thompson, M.C., 2018b. The effect of imposed rotary oscillation on the flow-induced vibration of a sphere. J. Fluid Mech. 855, 703–735.
Sareen, A., Zhao, J., Sheridan, J., Hourigan, K., Thompson, M.C., 2018c. Vortex-induced vibrations of a sphere close to a free surface. J. Fluid Mech. 846, 1023–1058.
Sarpkaya, T., 2004. A critical review of the intrinsic nature of vortex-induced vibrations. J. Fluids Struct. 19 (4), 389–447.
Singh, S., Mittal, S., 2005. Vortex-induced oscillations at low Reynolds numbers: hysteresis and vortex-shedding modes. J. Fluids Struct. 20 (8), 1085–1104.
Soti, A.K., Thompson, M.C., Sheridan, J., Bhardwaj, R., 2017. Harnessing electrical power from vortex-induced vibration of a circular cylinder. J. Fluids Struct. 70, 360–373.
Soti, A.K., Zhao, J., Thompson, M.C., Sheridan, J., Bhardwaj, R., 2018. Damping effects on vortex-induced vibration of a circular cylinder and implications for power extraction. J. Fluids Struct. 81, 289–308.
Wang, Z., Du, L., Zhao, J., Sun, X., 2017. Structural response and energy extraction of a fully passive flapping foil. J. Fluids Struct. 72, 96–113.
Wang, J., Geng, L., Ding, L., Zhu, H., Yurchenko, D., 2020. The state-of-the-art review on energy harvesting from flow-induced vibrations. Appl. Energy 267, 114902.
Wang, J., Wang, F., Li, J., 2025. Investigation of the influence of different incoming flow conditions on vortex-induced vibration in a 10: 1 rectangular section. Phys. Fluids 37 (5).
Williamson, C.H.K., Govardhan, R., 2004. Vortex-induced vibrations. Annu. Rev. Fluid Mech..
Yogeswaran, V., Sen, S., Mittal, S., 2014. Free vibrations of an elliptic cylinder at low Reynolds numbers. J. Fluids Struct. 51, 55–67.
Zhao, J., Hourigan, K., Thompson, M.C., 2018a. Flow-induced vibration of D-section cylinders: an afterbody is not essential for vortex-induced vibration. J. Fluid Mech. 851, 317–343.
Zhao, J., Hourigan, K., Thompson, M.C., 2019a. Dynamic response of elliptical cylinders undergoing transverse flow-induced vibration. J. Fluids Struct. 89, 123–131.
Zhao, J., Leontini, J.S., Lo Jacono, D., Sheridan, J., 2014. Fluid–structure interaction of a square cylinder at different angles of attack. J. Fluid Mech. 747, 688–721.
Zhao, J., Leontini, J.S., Lo Jacono, D., Sheridan, J., 2019b. The effect of mass ratio on the structural response of a freely vibrating square cylinder oriented at different angles of attack. J. Fluids Struct. 86, 200–212.
Zhao, J., Lo Jacono, D., Sheridan, J., Hourigan, K., Thompson, M.C., 2018b. Experimental investigation of in-line flow-induced vibration of a rotating cylinder. J. Fluid Mech. 847, 664–699.
Zhao, J., Nemes, A., Lo Jacono, D., Sheridan, J., 2018c. Branch/mode competition in the flow-induced vibration of a square cylinder. Philos. Trans. R. Soc. Lond. A 376, 20170243.
Zhao, J., Thompson, M.C., Hourigan, K., 2022. Damping effect on transverse flow-induced vibration of a rotating circular cylinder and its implied energy harvesting performance. Phys. Rev. Fluids 7 (2), 023905.